

Article

Kinematics and Controlling Factors of Slow-Moving Landslides in Central Texas: A Multisource Data Fusion Approach

Esayas Gebremichael ^{1,*}, Rosbeidy Hernandez ¹, Helge Alsleben ¹, Mohamed Ahmed ², Richard Denne ¹
and Omar Harvey ¹

¹ Department of Geological Sciences, Texas Christian University, Fort Worth, TX 76109, USA; r.denne@tcu.edu (R.D.); omar.harvey@tcu.edu (O.H.)

² Center for Water Supply Studies, Department of Physical and Environmental Sciences, Texas A&M University-Corpus Christi, Corpus Christi, TX 78412, USA; mohamed.ahmed@tamucc.edu

* Correspondence: e.gbremichael@tcu.edu

Abstract: The Austin metropolitan area has experienced unprecedented economic and population growth over the past two decades. This rapid growth is leading communities to settle in areas susceptible to landslides, necessitating a comprehensive analysis of landslide risks and the development of early warning systems. This could be accomplished with better confidence for slow-moving landslides, whose occurrences could be forecasted by monitoring precursory ground displacement. This study employed a combination of ground- and satellite-based observations and techniques to assess the kinematics of slow-moving landslides and identify the controlling and triggering factors that contribute to their occurrence. By closely examining landslide events in the Shoal Creek area, potential failure modes across the study area were inferred. The findings revealed that landslide-prone areas are undergoing creep deformation at an extremely slow rate (up to -4.29 mm/yr). These areas lie on moderate to steep slopes ($>22^\circ$) and are predominantly composed of clay-rich units belonging to the Del Rio and Eagle Ford formations. Based on the incidents at Shoal Creek, episodes of intense rainfall acting on the landslide-prone areas are determined to be the main trigger for landslide processes in the region.

Keywords: precursory deformation; slow-moving landslides; clay; early warning; rainfall; InSAR



Citation: Gebremichael, E.; Hernandez, R.; Alsleben, H.; Ahmed, M.; Denne, R.; Harvey, O. Kinematics and Controlling Factors of Slow-Moving Landslides in Central Texas: A Multisource Data Fusion Approach. *Geosciences* **2024**, *14*, 133. <https://doi.org/10.3390/geosciences14050133>

Academic Editors: Deodato Tapete and Jesus Martinez-Frias

Received: 1 April 2024
Revised: 2 May 2024
Accepted: 6 May 2024
Published: 14 May 2024



Copyright: © 2024 by the authors. Licensee MDPI, Basel, Switzerland. This article is an open access article distributed under the terms and conditions of the Creative Commons Attribution (CC BY) license (<https://creativecommons.org/licenses/by/4.0/>).

1. Introduction

Landslide phenomena can cause significant economic, human, and environmental losses. Landslides are categorized based on the materials involved and their rate of motion downslope [1–4]. Weak materials, such as clay-rich zones, create favorable conditions for initiating landslides, particularly slow-moving slides [5,6]. The velocities of slow-moving landslides can range from a few millimeters to tens of meters per year [5,7]. The kinematics of landslides with the latter displacement rates are mostly controlled by external factors, such as rainfall and seismic activity. These factors lead to an exponential decline in the shear strength of the landslide material, resulting in accelerated ground velocity that causes slope failures [8,9].

Forecasting the occurrence of fast-moving landslides poses a significant challenge due to their varying spatial scales, temporal patterns, modes of displacement, and complex interactions between slope material and controlling factors [5,10,11]. Most studies and early warning systems focus on applying various techniques to identify areas prone to all types of landslides through susceptibility mapping [12,13]. Commonly used techniques include heuristic, statistical, and deterministic methods [14–18]. Although several studies assessing the accuracy of these models have reported reasonably acceptable validation scores [19,20], these models suffer from limitations that constrain their accuracy and reliability. These limitations include the unavailability of datasets representing the parameters assessed in the susceptibility models, variations in the spatial resolution of multisource datasets requiring

resampling procedures to generate pseudocompatible datasets during data fusion, and the models' tendency to focus on shallow parameters while overlooking deeper processes and localized variations [20].

However, several studies have demonstrated the reliability of forecasting the failure of slow-moving landslides through long-term monitoring of precursory failure indicators, such as slow slope displacement processes, using data obtained from permanent or campaign global navigation satellite system (GNSS) surveys, inclinometers, extensometers, and other in situ instruments [21,22]. These studies have provided valuable insights into understanding the pre-failure kinematics of landslides, enabling more accurate forecasting of their occurrence [23–25]. However, the high cost of these instruments, coupled with the extensive time and labor requirements, make their application in monitoring and forecasting large-scale landslides impractical [26].

Fortunately, the growing capabilities of remote sensing instruments onboard satellite and aerial platforms, along with the availability of freely accessible satellite data with varying spatial and temporal resolutions, have made it easier for the public to access and utilize datasets and tools for investigating landslide processes [27]. Specifically, the use of interferometric synthetic aperture radar (InSAR) techniques applied to SAR datasets has proven effective in detecting centimeter- to millimeter-scale deformation rates, indicating active processes initiated by subsurface processes [28]. These techniques are widely employed to monitor subtle pre-failure deformation rates, which serve as precursors for identifying slow-moving landslides, enabling the development of early warning systems [29–33]. In most cases, landslide forecast models derived from remote sensing techniques are integrated with ground-based observations for calibration and validation, thereby improving the quality and reliability of the resultant products [34,35].

This study integrated multisource ground- and satellite-based observations and techniques to assess the kinematics of slow-moving landslides in Central Texas. Furthermore, an examination of the controlling factors and triggers that induce slope failures in the region was conducted by closely inspecting a site with a history of recurrent episodes of such failures in recent years.

2. The Study Area

The study investigates sections of the city of Austin and its surrounding areas in Travis County in Central Texas (Figure 1). The Greater Austin Metropolitan Area has experienced unprecedented growth in the past decade and is currently inhabited by over 2 million people [36]. Like other regions worldwide facing rapid population growth and urbanization, factors that amplify hazard susceptibility [37], the high rate of population growth in the Austin metropolitan area has resulted in the expansion of communities into naturally hazard-prone areas [36,38]. Moreover, the population and economic growth in the metropolitan area have led to intensified anthropogenic activities and associated changes, exacerbating the risks of natural hazards, particularly slope failures, on the community and the environment. Two major landslide events that occurred near residential properties in the same location in the Pease Park area of Austin, along Shoal Creek, in May 2018 and May 2019 (Figures 1 and 2) demonstrated the increasing susceptibility of communities to the hazard [39]. Multitemporal imagery of the impacted area, accessible through the time-lapse feature on the open-access Google Earth app (<https://earth.google.com/>, accessed on 20 November 2022), revealed that the area has undergone significant anthropogenic changes, including new property development, expansion, modifications to existing properties, and road construction over the past few decades. The landslides consequently caused damage to both public and private property and the surrounding environment, which are projected to cost the city substantial investment (more than \$20 million) for repair and mitigation efforts [39].

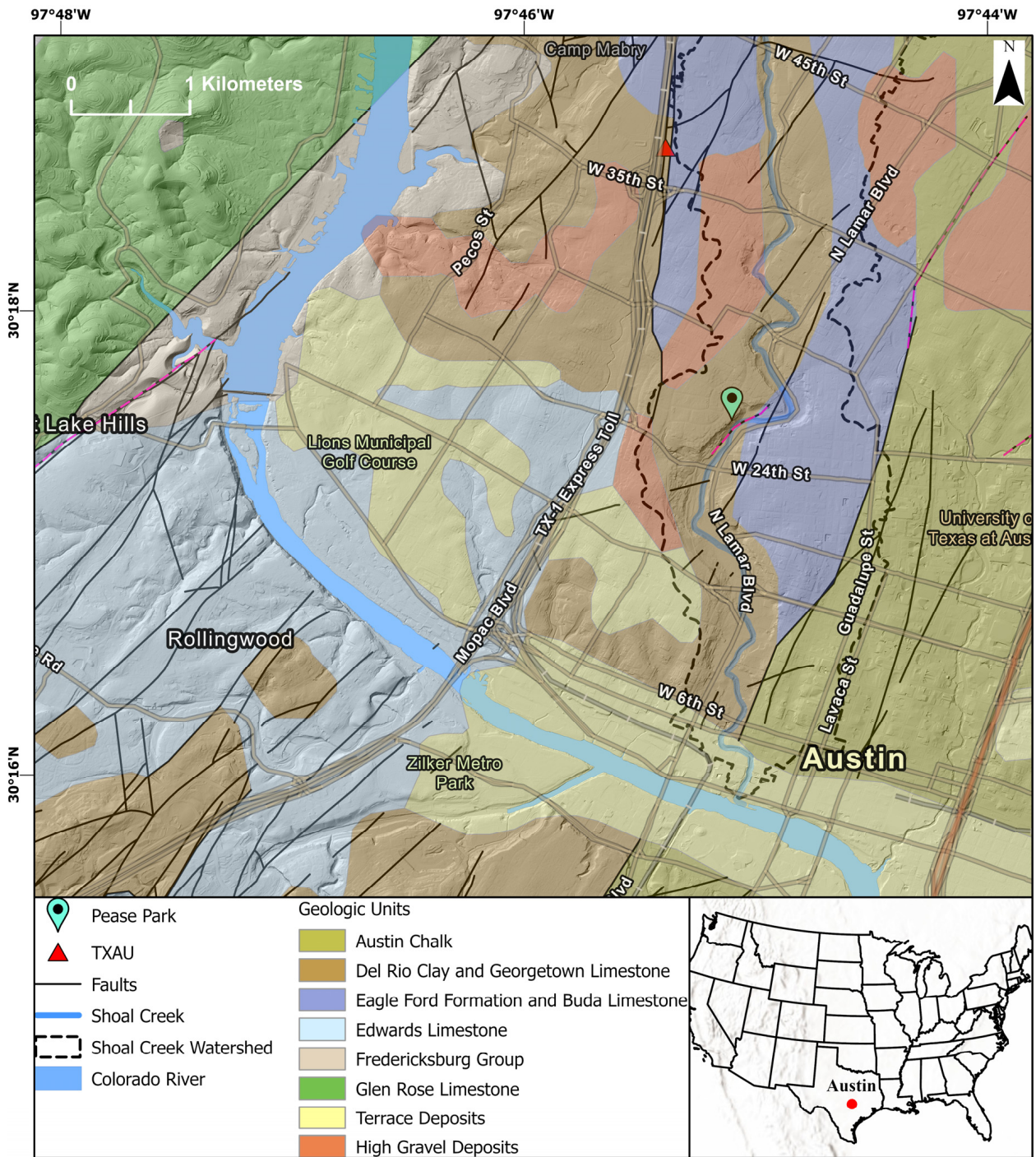


Figure 1. Geographic and geologic setting of the study area. Also shown are Pease Park (light blue pin), where recent landslides occurred, Shoal Creek and its watershed (blue and dashed black line, respectively), the Colorado River, and the TXAU GNSS station (red triangle).

It is believed that this study is the first to attempt to investigate the kinematics of the landslides in the study area and provide a comprehensive assessment of the factors that contribute to their occurrence.

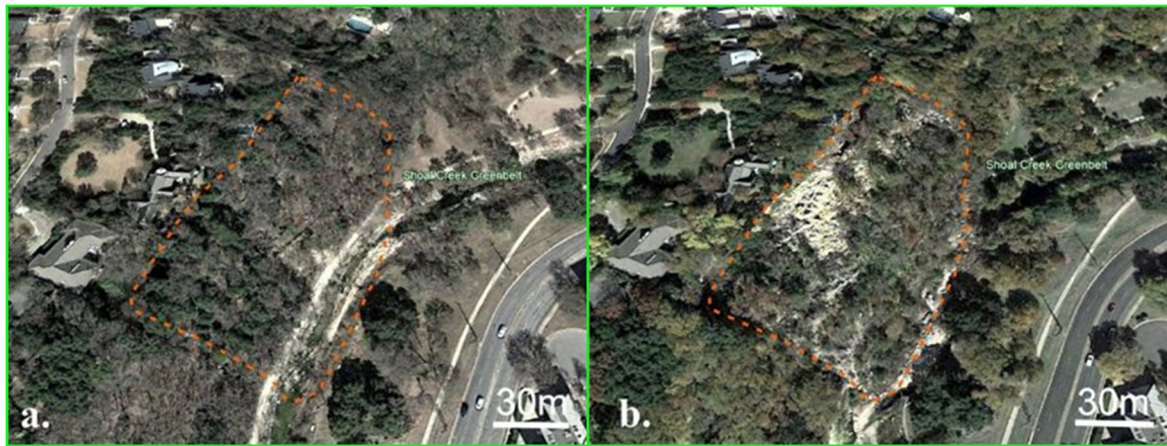


Figure 2. Google Earth images of the Pease Park slope failure site (shown in dashed orange lines) (a) before and (b) after the first slope failure event (2018).

Climatic and Geologic Settings

The climate of the study area is described as a humid subtropical climate, featuring long, moderately hot summers and mild winters. The area experiences moderate precipitation, with average annual values ranging from 810 mm to 910 mm [40].

The Balcones Fault Zone (BFZ) represents the main structural feature in the study area. It consists of a system of normal faults that strike NE–SW and predominantly dip southeastward (Figure 1). This fault zone, which is no longer active, occurs at the western boundary of the study area and in areas close to Shoal Creek, exerting primary control over the spatial distribution of rock formations (Figure 1) [41].

Within the study area, the predominant geological formations are sedimentary rocks, ranging in age from the Early to Late Cretaceous (Figure 1). Additionally, unconsolidated Quaternary sediments such as terrace and alluvial deposits are common. The rock formations found on the eastern, downthrown side of the fault zone (in the study area) are Upper Cretaceous shales and chinks that dip gently to the east, including the Eagle Ford Shale and Austin Chalk. The western, upthrown fault block is composed of Lower Cretaceous limestones, including the Glen Rose, and the Edwards and Walnut formations (Fredericksburg Group) (Figure 1). These limestones mainly consist of hard limestone layers interbedded with softer marly/clay-rich layers [41–44].

The Del Rio, Buda, and Eagle Ford formations are of particular interest, as they constitute the dominant formations in Shoal Creek and surroundings in general, including Pease Park, where recent recurrent landslide events have been reported (Figure 2). Understanding the geological conditions at the slope failure site is crucial, as it could provide valuable insight into the mechanisms behind landslides throughout the entire investigated region. The Del Rio Clay is a laminated, calcareous, and gypsiferous mudstone with varying amounts of pyrite [45]. The clay in the Del Rio Formation exhibits a shrink–swell behavior and is primarily composed of montmorillonite, smectite, and kaolinite, with minor amounts of illite [43,46,47]. These minerals exhibit very low shear strength when saturated with water [48].

Overlying the Del Rio Clay is the Buda Limestone, previously referred to as the “Shoal Creek limestone” in early literature [49]. The Buda Limestone, which generally forms steep slopes above the Del Rio Clay, is the dominant unit found on the high cliffs of Shoal Creek [50] (Figure 1). It is characterized as a fine-grained, bioclastic, pyritiferous limestone that is generally hard and brittle but exhibits less resistance in certain sections, particularly in the lower part where bioerosion structures are more prevalent. The Buda Limestone is relatively thin in the Central Texas region, ranging from 11 to 16 m in thickness within the study area [45,46,51,52]. The Buda Limestone is capped by the Eagle Ford Shale which also contains in its lower part siltstone, very fine sandstone, and a significant amount of smectite clay [53].

3. Materials and Methods

This study integrates multisource datasets and results generated through various techniques applied to the datasets to accomplish two objectives: (1) detect slow-moving landslides whose occurrences can be forecasted based on precursory displacement patterns and (2) identify the controlling factors and triggers that govern the incidence of these landslides in the study area.

3.1. Detecting Slow-Moving Landslides

3.1.1. Small Baseline Subset (SBAS) Interferometric Technique

The SBAS technique was chosen in this study to identify targets whose movement could potentially be induced by slow-moving landslide processes. The SBAS method involves stacking multiple interferograms created from multitemporal SAR imagery with small spatial and temporal baselines. This stacking process produces a cumulative deformation rate [54–56]. Initially, the interferograms were multilooked to enhance their signal-to-noise (SNR) ratios, unwrapped, and then stacked together. Pixels that exhibit temporal coherence in all interferograms are inverted to estimate line-of-sight (LOS) velocities [54,57]. In the subsequent step, the LOS velocities were geocoded and reprojected to produce vertical displacement (VD) values. Positive and negative displacement rates indicate movement of the target surface toward and away from the satellite in the repeat observations, respectively [58].

Fifty-three interferometric wide (IW) swath mode level-1 single look complex (SLC) SAR images acquired, along the ascending track, between March 2015 and January 2021 by the Sentinel-1 mission (Figure 3) were used to quantify subtle deformation rates associated with slow-moving landslides. The image acquired on 2 February 2019 was chosen as the super reference scene (shown in yellow marker in Figure 3). This image served as a reference for aligning all the other images to its geometry—a procedure referred to as coregistration. Due to the limited availability of level-1 IW mode SLC images via the Alaska Satellite Facility's (ASF) data dissemination platform (<https://vertex.daac.asf.alaska.edu/>, accessed on 2 February 2021), only the VD component of the landslide motion viewed from the perspective of the ascending geometry was used in this study for analysis and interpretation. The SBAS workflow within the SARscape Module of ENVI 5.5 was employed for data processing and result generation.

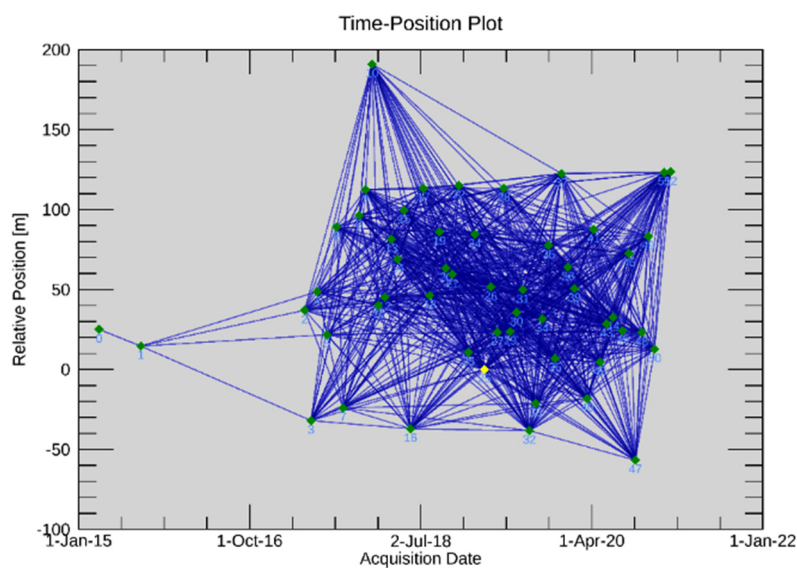


Figure 3. Time–position plot illustrating the temporal and spatial baseline information of the SAR image combinations (shown as green markers).

3.1.2. Calibration Using GNSS Data

Two GNSS datasets obtained through different geodetic techniques were utilized in this study to calibrate and validate the SBAS results. The first set of geodetic data for the study area was acquired from a permanent GNSS station (TXAU; red triangle in Figure 1) that continuously measures displacement rates over a longer time scale and can detect subtle (mm-scale) deformation rates. The analysis results of the TXAU permanent GNSS station data, obtained from the Nevada Geodetic Laboratory data distribution platform [59], were further analyzed in tandem with the SBAS analysis result for calibration purposes. The TXAU station was chosen for this purpose due to its extensive daily position data coverage from 1996 to 2021. Calibration of the SBAS rates was conducted using the average vertical displacement rates from the TXAU station, following the procedures outlined by Emil et al. (2021) and Haley et al. (2022) [60,61]. In this study, a 100-m radius buffer surrounding the TXAU station was generated, and the mean deformation rates derived using the SBAS method within the buffer polygon were obtained. The discrepancy between the vertical deformation value of the mean SBAS pixels within the 150-m distance and the TXAU deformation rates was utilized to correct the displacement rates of all pixels derived using the SBAS technique.

Additionally, two GNSS displacement measurement campaigns were conducted in August 2021 and March 2022. The sites for the survey were selected by identifying areas that exhibited relatively low to moderate negative deformation rates (away from the satellite) in the SBAS results. Sites immediately adjacent to the Pease Park landslide area (indicated by a light blue pin in Figure 1) that met these criteria were chosen for the campaign investigation. The data was collected using the Emlid Reach RS2 GNSS unit, consisting of the base station and rover receivers and the real-time kinematic (RTK) GNSS survey approach [62].

3.2. Identifying Processes and Factors That Induce Slow-Moving Landslides

3.2.1. Thematic Datasets

Three thematic datasets and analysis results were assessed to identify the processes and factors governing the occurrence of slow-moving landslides in the study area. The datasets considered were slope gradient, local geology, and geological structures. These parameters were overlaid on a deformation distribution (density) map to observe their spatial correlation.

A light detection and ranging (LiDAR)-derived high-resolution (1 m) DEM dataset obtained from the Texas Geographic Information Office (<https://geographic.texas.gov/>, accessed on 20 November 2022) was utilized to calculate the slope. The slope values, measured in degrees ($^{\circ}$), represented the maximum rate of vertical change between each pixel and its neighboring pixels. The results were classified into five categories using the Jenks optimization algorithm for visualization and result interpretation purposes: less than 4° , $4\text{--}11^{\circ}$, $11\text{--}22^{\circ}$, $22\text{--}38^{\circ}$, and greater than 38° .

The stability of slow-moving landslides is strongly influenced by the lithologic composition and tectonic setting of the area [63,64]. Therefore, special attention was given to the geology and tectonic features in the study area. The impact of faults and other geological structures on slope failures is twofold. First, stress buildup in active geological structures can induce slope instability by disturbing and weakening the cohesion of geological materials, thereby reducing shear strength [5,65]. Second, geological structures can act as conduits for transferring water from the surface to deeper layers. The interaction between water and these layers may initiate processes that ultimately lead to slope failure [66]. Therefore, the proximity of geologic units to geological structures increases the probability of slope failures [67]. Geological information for the study area (Figure 1), including detailed descriptions of lithologic units and the spatial distribution of tectonic features, was obtained from the United States Geological Survey [USGS] online data distribution platform (<https://www.usgs.gov/>, accessed on 20 November 2022) and also adapted from a previous study [46]. Additionally, single Sentinel-1 (level-1) data acquired during cloud- and rainfall-free tropospheric conditions (1 August 2021)

was analyzed using the open-source Sentinel Application Platform (SNAP v8.0) software to complement the mapping of geological structures in the study area. This was done to identify structures that may not have been detected using conventional methods in previous mapping studies. The methodology outlined by Tagnon et al. (2020) [68] was adopted for delineating linear structures associated with faults and fractures. In this method, geological features were manually delineated by observing changes in the backscatter intensity of SAR images after applying adaptive filters. These filters removed speckles and other noises, enhancing the sharpness and details of the SAR images to highlight lineaments that could be interpreted as fractures or faults. The high-spatial-resolution DEM data of the study area was integrated into the delineation exercise to further supplement and refine the SAR-based structural mapping technique. Once the lineaments were identified, the newly mapped structures were overlaid on the known structures to establish spatial correspondence. The underlying premise is that if there is a spatial agreement between the existing faults in both maps (structures from the geological map and the SAR-derived structural map), it validates the reliability of the method and confirms the accuracy of the newly mapped structures.

3.2.2. Ancillary Data and Methods—3D Model from Unmanned Aerial Vehicle (UAV) Data

A close investigation of the geometry and geology of the recent failure site was proposed in this study to comprehend the mechanisms behind the formation of the landslide and validate the hypothesized mechanism of landslide formation in the study area proposed in this research. Due to the large spatial scale of the landslide event in the Pease Park area (>8000 m² in surface area), coupled with its inaccessibility, observing the entire area and gathering detailed information on the landslide's geometry was not feasible. However, a closeup investigation of the area became possible by generating a 3D model of the landslide geometry, achieved through the application of the structure from motion (SfM) algorithm to high-resolution imagery captured by the DJI Spark Unmanned Aerial Vehicle (UAV). The SfM procedure was facilitated using the cloud-based DroneDeploy software (v 2.0.44).

4. Results and Discussion

This section describes the results obtained using the datasets and methods outlined in Section 3. Additionally, it provides an in-depth assessment of the displacement mechanisms of potential landslide sites, controlling factors, and triggers. This is accomplished through conceptualization of the processes and factors that led to the incidence of landslides at the Pease Park (Shoal Creek) site.

4.1. Active Slow-Moving Displacement

The deformation rate obtained through the SBAS analysis technique was calibrated using the deformation rate (-0.99 ± 0.55 mm/yr [1996–2021]) derived from the TXAU permanent station (Figures 1 and 4) employing the method described in Section 3.1.2. Following the calibration procedure, the ground deformation velocity values (99.8% of the values) within the study area (Figure 4) ranged from +1.80 mm/yr to -4.80 mm/yr, with a mean (and standard deviation, respectively) deformation rate of -1.7 ± 0.7 mm/yr.

The present study focuses on assessing negative deformation rates, which signify movement of the slope material away from the satellite in a vertical direction, henceforth simply called deformation, to identify various deformation patterns related to landslides and other processes in the study area.

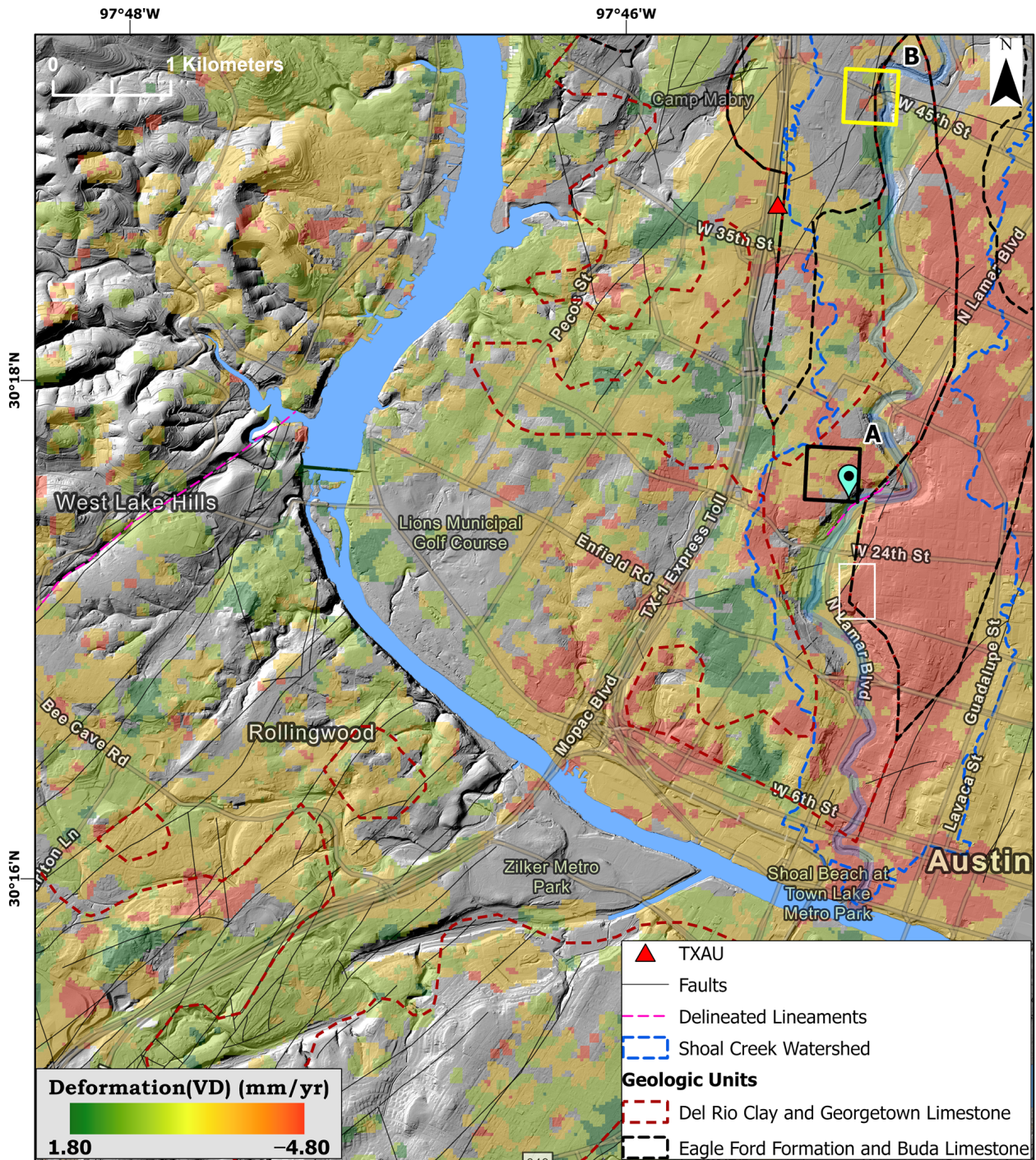


Figure 4. VD displacement rate (mm/yr) in the study area determined using the SBAS technique. The landslide site in the Pease Park (where multitemporal GNSS surveys were conducted), as well as another site investigated during the field survey, is represented by black-outlined (A) and yellow-outlined (B) polygons, respectively.

The majority of the study area (~68%) exhibits deformation rates ranging from -2 mm/yr to $+1.8$ mm/yr (Figure 4). These rates correspond spatially with the distribution of the Lower Cretaceous Edwards and Glen Rose limestones as well as the Upper Cretaceous Austin Chalk (Figures 1 and 4). Relatively moderate rates of hillslope deformation (-2 to -3.91 mm/yr) were observed at several locations along the cliffs of Shoal Creek, primarily composed of the Del Rio Clay (indicated by the dashed brown polygon in Figure 4) with a thin overlay of Buda Limestone. Pockets of relatively high deforma-

tion rates (up to -4.29 mm/yr; Figure 4) were observed in the cliffs opposite Shoal Creek (near North Lamar Boulevard), where the dominant geological formation is the Eagle Ford, overlaying the Buda Formation (indicated by the dashed black polygon in Figure 4). Deformation rates up to -4.4 mm/yr were observed in the central/downtown Austin City area. This area is underlain by the Eagle Ford Formation and Buda Limestone, containing clastic and clay layers (Figures 1 and 4). As observed in many urban settings underlain by clastic/recent sediments and weak units, the relatively moderate to high deformation rates observed in these areas could be attributed to compaction-induced deformation (or changes in the morphology of weak units) resulting from increased stress and loading applied to the ground surface from buildings and other artificial structures [69]. Small clusters (some as small as under 100 m²) exhibiting relatively high deformation rates (up to <-4.8 mm/yr) (Figure 4) were detected in the northeastern and central parts of the study area. During field investigation of several randomly chosen sites located outside the Shoal Creek area and undergoing relatively high deformation rates (e.g., area depicted by the white-outlined polygon in Figure 4), it was observed that new property development was ongoing or recently completed, as evidenced by time-lapse imagery of an area in Google Earth Pro from 2017 to 2021 (Figure 5). The observed relatively high deformation rates in these areas may be linked to accelerated compaction of newly added soil material for construction projects. These findings suggest that not all displacement signals shown in Figure 4 can be solely attributed to active landslide processes.



Figure 5. Time-lapse imagery ((a): February 2017; (b): June 2021) of an area (shown in a white-outlined polygon in Figure 4) undergoing deformation at a rate of -4.2 mm/yr, attributed to other (non-landslide) processes.

Studies indicate that deformation rates exceeding -2 mm/yr do not significantly contribute to the incidence of landslides. The value also represents the noise threshold of the accuracy of displacement estimate using InSAR techniques [30,70,71]. Hence, this research used deformation rates of -2 mm/yr and lower as a potential indicator/metric for identifying active or reactivated slow-moving landslides in the study area. Bianchini et al. [30] argued that using lower thresholds ensures that active or reactivated landslides undergoing deformation at a very slow rate but that could eventually transition into devastating landslides are identified. For instance, several studies used <-1.5 mm/yr threshold to identify slow-moving landslides in Italy [72,73].

In the following sections, various controlling factors and triggers for the incidence of landslides in the study area are discussed at length, focusing on the Shoal Creek area, particularly Pease Park, where recent events have transpired. The goal is to provide a conceptual model of the kinematics and mechanisms of slope failure in the study area and determine the driving factors.

Landslide Activity at Shoal Creek

A segment of Shoal Creek, specifically a site in the Pease Park area (shown in blue pin in Figure 4), has experienced two consecutive rotational landslide events in recent years following heavy rainfall episodes [74,75]. The first event, which caused significant displacement approximately 300 feet in length [74], occurred in May 2018, followed by a minor debris movement the following year in May 2019 [75]. The daily precipitation records for May in both 2018 and 2019 (Figure 6), obtained from a station (ID: GHCND:US1TXTV0044; source: National Environmental Satellite, Data, and Information Service (<https://www.ncei.noaa.gov/>, accessed on 1 March 2024) located near Pease Park in the Shoal Creek area, indicate the prevalence of relatively high daily rainfall totals (up to 101 mm in the case of the May 2018 event) before the onset of debris movement along Pease Park (Figure 6). Historical records also provide evidence of similar slope failures occurring in various sections of the Shoal Creek area decades before the recent events [76].

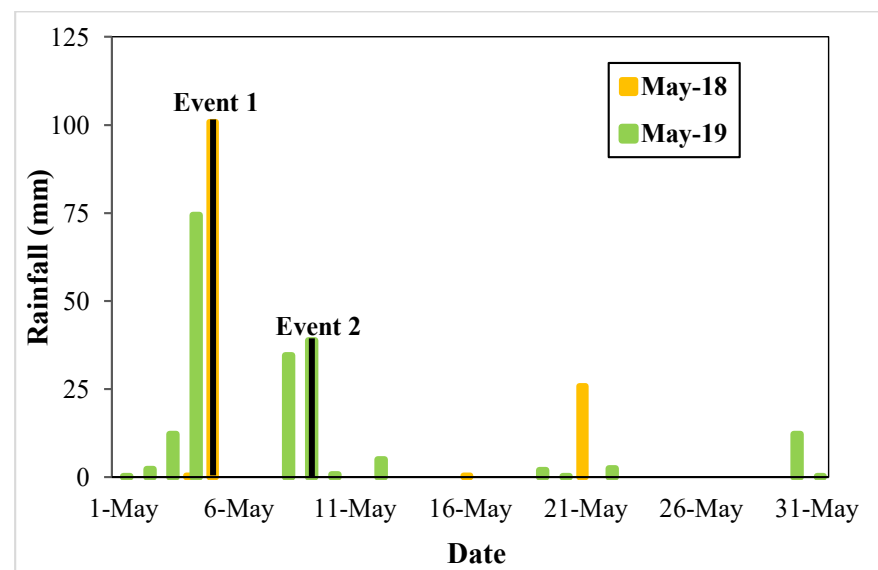


Figure 6. Graph showing the daily precipitation records for May 2018 (shown in yellow) and May 2019 (shown in green). Also shown are the onset times of the landslide events (events 1 and 2).

Although the SBAS analysis did not detect active displacement on the cliff of the recent failure site of the creek due to the expected loss of interferometric coherence resulting from changing surface conditions following the landslide event [77], deformation rates from the surrounding pixels (black-outlined polygon (label A) in Figure 4) indicate an active, though extremely slow (-2.24 ± 0.19 mm/yr) per the classification by Cruden and Varnes (1996) [78], hillslope deformation process. This indicates that the landslide at the recent site was the result of very slow slope displacement activity that gradually morphed into slope failure due to triggering factors and conducive settings for slope failure (discussed below). Furthermore, other physical indicators observed during the field investigations (discussed below) also support the assessment that the ground surface in the Pease Park area is continuously in motion. To further validate this active designation of the Pease Park slope, and since there are no permanent GNSS stations near the recent failure site (in Pease Park (Figure 4)), deformation activity and rates over the flanks of the failure site

(Figures 1 and 4) were estimated using the RTK GNSS measurement technique during two field campaigns: one in August 2021 and another in March 2022. The analysis of the multitemporal campaign GNSS data indicated that the hillslope is undergoing active and relatively high deformation activity (up to -17 mm/month). It is important to note that the March 2022 RTK GNSS campaign was conducted under dense cloud cover conditions and following an intense rainfall event the previous day, which caused slight movement of the landslide debris downslope and resulted in accessibility issues at all but one of the sites from the August 2021 RTK GNSS campaign. The results showed a relatively higher deformation rate (up to -17 mm/month) than that reported by the SBAS analysis (of nearby pixels); however, this can be attributed partially to the effect of clouds or precipitation on the GNSS signal [79] during the second measurement, a displacement rate accelerated by the intense precipitation episode in the days before the field visit, or the relatively short duration of the investigation. Nonetheless, these results demonstrated ongoing activity in the area, as depicted by the SBAS pixels from nearby sites (Box A in Figure 4).

This assessment consolidates the notion that slope materials in the study area undergoing deformation at a rate of less than -2 mm/yr, as indicated by the SBAS result (Figure 4), are likely experiencing active slow-moving landslide activity. This activity could eventually culminate in slope failure if triggering events occur and conditions for the controlling factors are met.

4.2. Slope and Tectonic Features

A slope map, generated using the LiDAR DEM data (Figure 7), revealed gradient angles ranging from 0° to 86° . Elevations over 96% of the study area exhibit a maximum slope gradient of 22° . According to Highland and Bobrowsky [7] and Zhang et al. [80], slow-moving landslides such as slides and creeps are common in slope angles ranging approximately between 20° and 50° . Hence, for examining the spatial relationship between relatively moderate to steep slope topography and slow-moving landslides in the study area, slope angles falling within the ranges of 22 – 38° and greater than 38° were isolated from the classes of slope angles obtained using the natural break classification (Figure 7). These categories constitute approximately 3.21% and 0.64% of the slope values within the study area, respectively. Within the Shoal Creek Watershed, including Pease Park, more than 81% of the area is characterized by the relatively moderate slope angle class (22 – 38°). North of the Balcones Escarpment (Figure 7), both relatively moderate and steep slope values (exceeding 38°) were observed. Steep slope gradients were also noted in certain pockets along the Barton Creek area (southwestern part of the study area) and in proximity to the Colorado River pathways (Figure 7).

The Balcones Faults, and smaller localized faults, are predominantly concentrated in the southern part of the study area, adjacent to the Colorado River, with fewer occurrences to the north of the river (Figures 4 and 7). Some of these faults run parallel to or intersect Shoal Creek (Figures 4 and 7). By utilizing the methodology described in Section 3.2.1, the complementary mapping of faults revealed the existence of NE–SW trending faults/lineaments in various areas, including Pease Park and other regions within the study area (Figures 4 and 7). Notably, some of the delineated lineaments (indicated by dashed pink lines in Figure 4) spatially overlap with tectonic features identified in previous studies, such as a fault along the upper periphery of the BFZ near West Lake Hills (Figure 4). This overlap serves to demonstrate the accuracy and reliability of the lineaments mapped in this study.

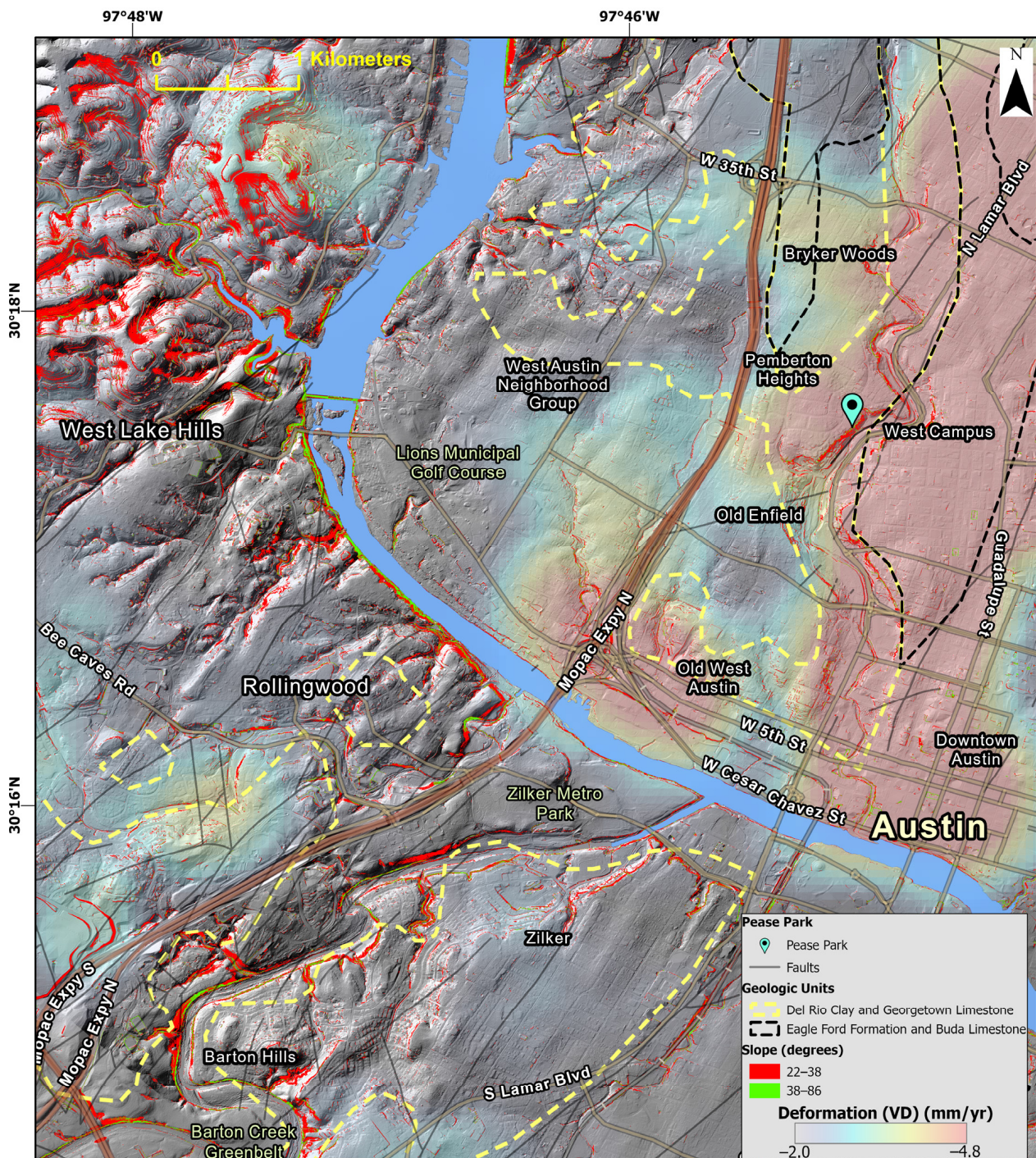


Figure 7. Slope (in degrees $^{\circ}$), geology, and faults superimposed on the deformation (<-2 mm/yr) density distribution map to identify the processes and factors that control the incidence of slow-moving landslides in the study area.

4.3. Landslide Type, Geometry, Kinematics, and Driving Factors

There is a spatial correlation between the (negative) VD deformation patterns, signifying slow-moving active landslides (<-2 mm/yr), and moderate to steep slope values ($>22^{\circ}$) in most terrains along Shoal Creek and to the north of the Colorado River in general (Figure 6). However, not all terrain with moderate to steep slopes may potentially experience slope failure incidents (Figure 7).

For example, the steep slope terrains north of the Balcones Escarpment (north of West Lake Hills [Figure 7]) exhibit some of the highest slope gradient values observed in the

study area ($>60^\circ$); however, they are not undergoing any significant and large-scale active displacement, per the SBAS-based deformation assessment, as areas along the downstream sections of the Colorado River (Figures 4 and 7).

Most of the moderately to steeply sloping terrains undergoing active displacement in the study area are underlain by the Eagle Ford and the Del Rio formations (Figure 7) and are dissected by or located proximal to faults belonging mostly to the Balcones Fault System. These facts indicate that geology and tectonic features, coupled with moderate to steep slope terrain conditions, are the leading controls for the incidence of landslides in the study area.

Drawing from observations of landslide geometry in the Pease Park area and other indicators across the Shoal Creek area, along with deformation patterns determined using fused SBAS–GNSS methods, a combination of two landslide types in the study area was identified. These types align with the landslide classification system by Highland and Bobrowsky [7] and Hungr et al. [2]: rotational slide (slump) and (rock) creep landslide types. A series of cascading events is thought to be the cause of slope failure at Pease Park and may serve as an analog for possible failure modes across other parts of the study area:

- The role of tectonic features: it is hypothesized that tectonic features of the Balcones Fault System and other faults cutting through the Buda Limestone acted as channels for infiltrating water/precipitation from the surface to the Del Rio Clay. The delineated lineament (dashed pink line in Figure 4) and other tectonic structures (discussed below) in the Pease Park area may have served as preferential pathways for water to infiltrate through the Buda Limestone.
- The role of local geology: water percolating through the fractured Buda and interacting with the montmorillonite-, smectite-, and kaolinite-rich Del Rio Formation induced clay swelling. This swelling translated to stress buildup at the landslide failure plane. Due to the brittle nature of the overlying Buda Limestone, the added stress resulted in the breaking up/fracturing of the Buda, subsequently leading to a decline in shear strength.
- Mechanisms of slope failure and driving factors: the Del Rio acted as a sliding surface, causing slow vertical and lateral displacement of the Buda Limestone. We believe that the area around Shoal Creek, which has undergone active deformation due to landslide activity, is experiencing ongoing mass movement. This movement is slow to very slow (creep), both vertically and laterally, with the Del Rio Formation acting as the sliding surface and the overlying shallow and weakened Buda Limestone sliding slowly downslope. The driving force and shear strength imbalance of the slope material induced by extreme rainfall episodes triggered movements that initiated the transition to rotational slumping on steep slopes. This scenario is supported by studies that show that intense rainfall episodes can further compound stress buildup through added pore pressure, leading to a decline in shear strength. In addition, changes in the saturation level of the landslide material, particularly in loose soil and weathered geologic units, compound the added stress applied to the slope material. These processes, in tandem, contribute to the driving force acting on the slope to exceed the shear strength of the material and, consequently, trigger landslides [81–83].
- Impact of anthropogenic land use–land cover changes: the loss of vegetation, that could anchor the landslide material, due to anthropogenic land use–land cover changes in the surrounding environment of Pease Park over the past few decades may have worsened the conditions that led to occurrence of landslides. Such changes may continue to have negative impacts on the detected susceptible areas and could contribute to the occurrence of landslides in the future.

A careful examination of the landslide geometry at Pease Park was made possible through the utilization of a 3D model of the cliff and its surroundings, which was generated using datasets acquired by UAV (Figure 8). The analysis revealed a curved and concave rupture surface, scarp, crown, and various other features associated with slumps. Moreover, it demonstrated a shallow failure zone, wherein the overlying Buda unit and underlying

Del Rio unit were found to have shallow contact, indicating that the Del Rio Clay unit functions as a slip surface. Additionally, the figure illustrates potential pathways (depicted by red lines in Figure 8) that could have facilitated the infiltration of precipitation to the underlying Del Rio mudstones during precipitation episodes.



Figure 8. 3D model of the Pease Park (Shoal Creek) landslide. The inset on the right side provides a close-up view of the contact between the Buda Limestone and the Del Rio layer, which acts as a slip surface. Several fracture pathways within the Buda Limestone, through which surface water may have percolated into the subsurface and interacted with the Del Rio Clay layer, are depicted in red.

Precursory surface geomorphic evidence of an active rock creep landslide process, such as holes and dips in the ground [84], had been observed by residents long before the slope failure in the Pease Park area [85]. This observation was further supported by the tilted or bent structure of trees (Figure 9a) encountered during the field investigation in the area.



Figure 9. Ongoing landslide process precursory indicators observed at (a) Pease Park and (b) another area within Shoal Creek located nearly two miles from Pease Park (location shown in yellow-outlined polygon in Figure 4).

Additionally, a similar geomorphic pattern, although in the early stages of morphing into a rotational slump, was identified at a location within Shoal Creek (yellow-outlined box (label B) in Figure 4) through an indicator of landslide activity observed during the field investigation. At this site, tension cracks (depicted as dashed black lines in Figure 9b), which are indicative of the initial phases of a shallow rotational slide [35,86], were observed. The site is situated on a moderate slope ($\sim 28^\circ$) and is experiencing deformation of up to -2.29 mm/yr based on the displacement rate of adjacent pixels. Similarly, the cliffs on the opposite side of Shoal Creek which are dominated by the smectite-rich Eagle Ford and dissected by faults (Figure 4) are potential sites of active slow-moving landslide processes. The sites lie at moderate to steep slopes ($>22^\circ$) and move at a VD rate of up to -4.29 mm/yr (Figure 4). Several studies focusing on south and central Texas corroborate this assessment of the susceptibility of cliffs dominated by the Eagle Ford Formation to slow-moving landslides [87–89].

5. Conclusions

This study employed an integrated approach, combining multisource remote sensing and in situ datasets and analysis results to evaluate landslide-prone areas in Austin City and its surroundings. This was principally achieved by investigating the landslide occurrence at the recent failure site in Shoal Creek as an analog model representing the kinematics, mechanisms, and processes that trigger landslides in the study area. The results indicated that the potential landslide sites are undergoing deformation at an extremely slow rate (up to -4.29 mm/yr). These areas are lithologically dominated by a thin layer of Buda Limestone underlain by the Del Rio Clay, as well as the Eagle Ford Shale overlying the Buda Limestone. These units are intersected by numerous NE–SW trending faults from the Balcones Fault System. Water/precipitation percolation through the tectonic features and interaction with the clay minerals at shallow depths are identified as factors that contribute to stress accumulation that leads to the reduction in shear strength. In this case, the clay layers act as a sliding surface, resulting in gradual (creep) vertical and lateral displacement of the Buda Limestone and Eagle Ford Formations, eventually transitioning into a rotational landslide under favorable slope conditions ($>22^\circ$) and triggered by episodes of intense rainfall. Considering the unprecedented population and economic growth of the Austin metropolitan area in recent years, understanding landslide-prone areas and identifying the triggering factors would facilitate the development of an early warning system for landslides in the region.

Author Contributions: Conceptualization, E.G. and R.H.; methodology, E.G., R.H., H.A., R.D. and O.H.; software, E.G. and R.H.; validation, E.G., R.H. and R.D.; formal analysis, E.G., R.H. and R.D.; writing—original draft preparation, E.G., R.H., H.A., R.D. and M.A.; writing—review and editing, E.G., R.H., H.A., M.A., R.D. and O.H. All authors have read and agreed to the published version of the manuscript.

Funding: This research received no external funding.

Data Availability Statement: The data utilized in this study are publicly available and accessible through the links provided in the article. The analysis results supporting the findings of this study can be obtained from the corresponding author upon reasonable request.

Conflicts of Interest: The authors declare no conflict of interest.

References

1. Glade, T.; Anderson, M.G.; Crozier, M.J. *Landslide Hazard and Risk*; Wiley: Hoboken, NJ, USA, 2005; Volume 807, ISBN 9780471486633.
2. Hungr, O.; Leroueil, S.; Picarelli, L. The Varnes Classification of Landslide Types, an Update. *Landslides* **2014**, *11*, 167–194. [[CrossRef](#)]
3. Varnes, D.J. Landslide Types and Processes. In *Landslides and Engineering Practice*; Highway Research Board Special Report: Washington, DC, USA, 1958; Volume 24, pp. 20–47.
4. Yilmaz, C.; Topal, T.; Süzen, M.L. GIS-Based Landslide Susceptibility Mapping Using Bivariate Statistical Analysis in Devrek (Zonguldak-Turkey). *Environ. Earth Sci.* **2012**, *65*, 2161–2178. [[CrossRef](#)]

5. Lacroix, P.; Handwerger, A.L.; Bièvre, G. Life and Death of Slow-Moving Landslides. *Nat. Rev. Earth Environ.* **2020**, *1*, 404–419. [[CrossRef](#)]
6. Zerathe, S.; Lacroix, P.; Jongmans, D.; Marino, J.; Taïpe, E.; Wathélet, M.; Pari, W.; Smoll, L.F.; Norabuena, E.; Guillier, B.; et al. Morphology, Structure and Kinematics of a Rainfall Controlled Slow-Moving Andean Landslide, Peru. *Earth Surf. Process Landf.* **2016**, *41*, 1477–1493. [[CrossRef](#)]
7. Highland, L.M.; Bobrowsky, P. *The Landslide Handbook—A Guide to Understanding Landslides*; US Geological Survey: Reston, VA, USA, 2008.
8. Bayer, B.; Simoni, A.; Mulas, M.; Corsini, A.; Schmidt, D. Deformation Responses of Slow Moving Landslides to Seasonal Rainfall in the Northern Apennines, Measured by InSAR. *Geomorphology* **2018**, *308*, 293–306. [[CrossRef](#)]
9. Lacroix, P.; Perfettini, H.; Taïpe, E.; Guillier, B. Coseismic and Postseismic Motion of a Landslide: Observations, Modeling, and Analogy with Tectonic Faults. *Geophys. Res. Lett.* **2014**, *41*, 6676–6680. [[CrossRef](#)]
10. Coe, J.A. Regional Moisture Balance Control of Landslide Motion: Implications for Landslide Forecasting in a Changing Climate. *Geology* **2012**, *40*, 323–326. [[CrossRef](#)]
11. Intrieri, E.; Gigli, G. Landslide Forecasting and Factors Influencing Predictability. *Nat. Hazards Earth Syst. Sci.* **2016**, *16*, 2501–2510. [[CrossRef](#)]
12. Guzzetti, F. *Landslide Hazard and Risk Assessment*; Universitäts-und Landesbibliothek Bonn: Bonn, Germany, 2006.
13. Yang, Z.; Liu, C.; Nie, R.; Zhang, W.; Zhang, L.; Zhang, Z.; Li, W.; Liu, G.; Dai, X.; Zhang, D.; et al. Research on Uncertainty of Landslide Susceptibility Prediction—Bibliometrics and Knowledge Graph Analysis. *Remote Sens.* **2022**, *14*, 3879. [[CrossRef](#)]
14. Aleotti, P.; Chowdhury, R. Landslide Hazard Assessment: Summary Review and New Perspectives. *Bull. Eng. Geol. Environ.* **1999**, *58*, 21–44. [[CrossRef](#)]
15. Guzzetti, F.; Carrara, A.; Cardinali, M.; Reichenbach, P. Landslide Hazard Evaluation: A Review of Current Techniques and Their Application in a Multi-Scale Study, Central Italy. *Geomorphology* **1999**, *31*, 181–216. [[CrossRef](#)]
16. Kanungo, D.P.; Arora, M.K.; Sarkar, S.; Gupta, R.P. A Comparative Study of Conventional, ANN Black Box, Fuzzy and Combined Neural and Fuzzy Weighting Procedures for Landslide Susceptibility Zonation in Darjeeling Himalayas. *Eng. Geol.* **2006**, *85*, 347–366. [[CrossRef](#)]
17. Raghuvanshi, T.K.; Negassa, L.; Kala, P.M. GIS Based Grid Overlay Method versus Modeling Approach—A Comparative Study for Landslide Hazard Zonation (LHZ) in Meta Robi District of West Showa Zone in Ethiopia. *Egypt. J. Remote Sens. Space Sci.* **2015**, *18*, 235–250. [[CrossRef](#)]
18. Reichenbach, P.; Rossi, M.; Malamud, B.D.; Mihir, M.; Guzzetti, F. A Review of Statistically-Based Landslide Susceptibility Models. *Earth Sci. Rev.* **2018**, *180*, 60–91. [[CrossRef](#)]
19. Fleuchaus, P.; Blum, P.; Wilde, M.; Terhorst, B.; Butscher, C. Retrospective Evaluation of Landslide Susceptibility Maps and Review of Validation Practice. *Environ. Earth Sci.* **2021**, *80*, 485. [[CrossRef](#)]
20. Korup, O.; Stolle, A. Landslide Prediction from Machine Learning. *Geol. Today* **2014**, *30*, 26–33. [[CrossRef](#)]
21. Bordoni, M.; Vivaldi, V.; Boni, R.; Spanò, S.; Tararbra, M.; Lanteri, L.; Parnigoni, M.; Grossi, A.; Figini, S.; Meisina, C. A Methodology for the Analysis of Continuous Time-Series of Automatic Inclinometers for Slow-Moving Landslides Monitoring in Piemonte Region, Northern Italy. *Nat. Hazards* **2023**, *115*, 1115–1142. [[CrossRef](#)]
22. Wang, G.Q. Kinematics of the Cerca Del Cielo, Puerto Rico Landslide Derived from GPS Observations. *Landslides* **2012**, *9*, 117–130. [[CrossRef](#)]
23. Jiang, Y.; Luo, H.; Xu, Q.; Lu, Z.; Liao, L.; Li, H.; Hao, L. A Graph Convolutional Incorporating GRU Network for Landslide Displacement Forecasting Based on Spatiotemporal Analysis of GNSS Observations. *Remote Sens.* **2022**, *14*, 1016. [[CrossRef](#)]
24. Schulz, W.H.; McKenna, J.P.; Kibler, J.D.; Biavati, G. Relations between Hydrology and Velocity of a Continuously Moving Landslide—Evidence of Pore-Pressure Feedback Regulating Landslide Motion? *Landslides* **2009**, *6*, 181–190. [[CrossRef](#)]
25. Wang, J.; Nie, G.; Gao, S.; Wu, S.; Li, H.; Ren, X. Landslide Deformation Prediction Based on a GNSS Time Series Analysis and Recurrent Neural Network Model. *Remote Sens.* **2021**, *13*, 1055. [[CrossRef](#)]
26. Van Westen, C.J.; van Asch, T.W.J.; Soeters, R. Landslide Hazard and Risk Zonation—Why Is It Still so Difficult? *Bull. Eng. Geol. Environ.* **2006**, *65*, 167–184. [[CrossRef](#)]
27. Chen, T.H.K.; Prishchepov, A.V.; Fensholt, R.; Sabel, C.E. Detecting and Monitoring Long-Term Landslides in Urbanized Areas with Nighttime Light Data and Multi-Seasonal Landsat Imagery across Taiwan from 1998 to 2017. *Remote Sens. Environ.* **2019**, *225*, 317–327. [[CrossRef](#)]
28. Gebremichael, E.; Seyoum, W.M.; Ishimwe, B.; Sataer, G. Lake Surface Area Expansion: Insights into the Role of Volcano-Tectonic Processes, Lake Beseka, East Africa. *J. Hydrol. Reg. Stud.* **2022**, *41*, 101093. [[CrossRef](#)]
29. Bardi, F.; Raspini, F.; Ciampalini, A.; Kristensen, L.; Rouyet, L.; Lauknes, T.R.; Frauenfelder, R.; Casagli, N. Space-Borne and Ground-Based InSAR Data Integration: The Åknes Test Site. *Remote Sens.* **2016**, *8*, 237. [[CrossRef](#)]
30. Bianchini, S.; Cigna, F.; Righini, G.; Proietti, C.; Casagli, N. Landslide HotSpot Mapping by Means of Persistent Scatterer Interferometry. *Environ. Earth Sci.* **2012**, *67*, 1155–1172. [[CrossRef](#)]
31. Hu, X.; Bürgmann, R.; Fielding, E.J.; Lee, H. Internal Kinematics of the Slumgullion Landslide (USA) from High-Resolution UAVSAR InSAR Data. *Remote Sens. Environ.* **2020**, *251*. [[CrossRef](#)]
32. Intrieri, E.; Raspini, F.; Fumagalli, A.; Lu, P.; Del Conte, S.; Farina, P.; Allievi, J.; Ferretti, A.; Casagli, N. The Maoxian Landslide as Seen from Space: Detecting Precursors of Failure with Sentinel-1 Data. *Landslides* **2018**, *15*, 123–133. [[CrossRef](#)]

33. Jiao, Q.; Jiang, W.; Qian, H.; Li, Q. Research on Characteristics and Failure Mechanism of Guizhou Shuicheng Landslide Based on InSAR and UAV Data. *Nat. Hazards Res.* **2022**, *2*, 17–24. [[CrossRef](#)]
34. Carlà, T.; Tofani, V.; Lombardi, L.; Raspini, F.; Bianchini, S.; Bertolo, D.; Thuegaz, P.; Casagli, N. Combination of GNSS, Satellite InSAR, and GBInSAR Remote Sensing Monitoring to Improve the Understanding of a Large Landslide in High Alpine Environment. *Geomorphology* **2019**, *335*, 62–75. [[CrossRef](#)]
35. Casagli, N.; Frodella, W.; Morelli, S.; Tofani, V.; Ciampalini, A.; Intrieri, E.; Raspini, F.; Rossi, G.; Tanteri, L.; Lu, P. Spaceborne, UAV and Ground-Based Remote Sensing Techniques for Landslide Mapping, Monitoring and Early Warning. *Geoenvironmental Disasters* **2017**, *4*, 9. [[CrossRef](#)]
36. Bixler, R.P.; Yang, E.; Richter, S.M.; Coudert, M. Boundary Crossing for Urban Community Resilience: A Social Vulnerability and Multi-Hazard Approach in Austin, Texas, USA. *Int. J. Disaster Risk Reduct.* **2021**, *66*. [[CrossRef](#)]
37. Klimeš, J.; Escobar, V.R. A Landslide Susceptibility Assessment in Urban Areas Based on Existing Data: An Example from the Iguaná Valley, Medellín City, Colombia. *Nat. Hazards Earth Syst. Sci.* **2010**, *10*, 2067–2079. [[CrossRef](#)]
38. Lee, D.; Jung, J. The Growth of Low-Income Population in Floodplains: A Case Study of Austin, TX. *KSCE J. Civ. Eng.* **2014**, *18*, 683–693. [[CrossRef](#)]
39. Findell, E. City Council to Weigh Costly Shoal Creek Fix. *Austin American Statesman*. 2019. Available online: <https://www.statesman.com/story/news/politics/county/2019/06/18/costly-fix-to-shoal-creek-slope-to-come-before-city-council/4818786007/> (accessed on 20 November 2022).
40. Patil, V.; Bizcarguenaga, M.; Lieberknecht, K.; Felkner, J. Retrofitting Solutions for a Campus Building to Mitigate Urban Heat Island in a Hot Humid Climate. *J. Phys. Conf. Ser.* **2021**, *2042*. [[CrossRef](#)]
41. Brune, G.; Duffin, G.L. *Occurrence, Availability, and Quality of Ground Water in Travis County, Texas*; Texas Department of Water Resources: Austin, TX, USA, 1983.
42. Barnes, V.E.; Shell Oil, Co.; Humble Oil and Refining, Co.; Mobile Oil, Co.; Proctor, C.V.; Brown, T.E.; McGowen, J.H.; Waechter, N.B.; Eargle, D.H.; Baker, E.T.; et al. *Geologic Atlas of Texas: Austin Sheet*; University of Texas at Austin, Bureau of Economic Geology: Austin, TX, USA, 1981.
43. Clark, A.K.; Morris, R.E.; Pedraza, D.E. Geologic Framework and Hydrostratigraphy of the Edwards and Trinity Aquifers within Northern Medina County, Texas. *U.S. Geol. Surv. Sci. Investig. Map* **2020**, *2020*, 1–13. [[CrossRef](#)]
44. Young, K. *Guidebook to the Geology of Travis County*; Walter Geology Library: Austin, TX, USA, 1977.
45. Waechter, N.B.; Lozo, F.E.; Barnes, V.E. *Geological Atlas of Texas, Del Rio Sheet. Scale 1: 250000*; University of Texas at Austin, Bureau of Economic Geology: Austin, TX, USA, 1977.
46. Garner, L.E.; Young, K.P. *Environmental Geology of the Austin Area: An Aid to Urban Planning*; The University of Texas at Austin: Austin, TX, USA, 1976.
47. Kuniansky, E.L.; Ardis, A.F. *Hydrogeology and Ground-Water Flow in the Edwards-Trinity Aquifer System, West-Central Texas*; US Geological Survey: Reston, VA, USA, 2004.
48. Yalcin, A. The Effects of Clay on Landslides: A Case Study. *Appl. Clay Sci.* **2007**, *38*, 77–85. [[CrossRef](#)]
49. Davis, G.; Wilcox, G.; Arnone, M.; Bruington, S. Rejuvenating the Buda Limestone Reservoir in Texas by Using Crude Oil and Nitrogen Injection in Underbalanced Regime: Case History. In Proceedings of Society of Petroleum Engineers (SPE)/International Association of Drilling Contractors (IADC) 2016: Managed Pressure Drilling and Underbalanced Operations —Proceedings of the 2016 SPE/IADC Conference and Exhibition, Galveston, TX, USA, 12–13 April 2016.
50. Rodda, P.U. Geologic Map of the Austin West Quadrangle, Travis County, Texas. In *Virtual Landscapes of Texas*; University of Texas, Bureau of Economic Geology: Austin, TX, USA, 1970. [[CrossRef](#)]
51. Small, T.A.; Hanson, J.A.; Hauwert, N.M. *Geologic Framework and Hydrogeologic Characteristics of the Edwards Aquifer Outcrop (Barton Springs Segment), Northeastern Hays and Southwestern Travis Counties, Texas*; US Department of the Interior, US Geological Survey: Reston, VA, USA, 1996; Volume 96.
52. Valencia, F.L.; Laya, J.C.; Buatois, L.A.; Mángano, M.G.; Valencia, G.L. Sedimentology and Stratigraphy of the Cenomanian Buda Limestone in Central Texas, U.S.A.: Implications on Regional and Global Depositional Controls. *Cretac. Res.* **2022**, *137*. [[CrossRef](#)]
53. Dawson, W.C. Shale Microfacies-Eagle Ford Group (Cenomanian-Turonian) North-Central Texas Outcrops and Subsurface Equivalents. *Am. Assoc. Pet. Geol. Bull.* **2000**, *84*. [[CrossRef](#)]
54. Lanari, R.; Casu, F.; Manzo, M.; Zeni, G.; Berardino, P.; Manunta, M.; Pepe, A. An Overview of the Small Baseline Subset Algorithm: A DInSAR Technique for Surface Deformation Analysis. *Pure Appl. Geophys.* **2007**, *164*, 637–661. [[CrossRef](#)]
55. Berardino, P.; Fornaro, G.; Lanari, R.; Sansosti, E. A New Algorithm for Surface Deformation Monitoring Based on Small Baseline Differential SAR Interferograms. *IEEE Trans. Geosci. Remote Sens.* **2002**, *40*, 2375–2383. [[CrossRef](#)]
56. Crosetto, M.; Monserrat, O.; Cuevas-González, M.; Devanthéry, N.; Crippa, B. Persistent Scatterer Interferometry: A Review. *ISPRS J. Photogramm. Remote Sens.* **2016**, *115*, 78–89. [[CrossRef](#)]
57. Zhou, X.; Chang, N.-B.; Li, S. Applications of SAR Interferometry in Earth and Environmental Science Research. *Sensors* **2009**, *9*, 1876–1912. [[CrossRef](#)]
58. Sataer, G.; Sultan, M.; Emil, M.K.; Yellich, J.A.; Palaseanu-Lovejoy, M.; Becker, R.; Gebremichael, E.; Abdelmohsen, K. Remote Sensing Application for Landslide Detection, Monitoring along Eastern Lake Michigan (Miami Park, MI). *Remote Sens.* **2022**, *14*, 3474. [[CrossRef](#)]
59. Blewitt, G.; Hammond, W.; Kreemer, C. Harnessing the GPS Data Explosion for Interdisciplinary Science. *Eos* **2018**, *99*. [[CrossRef](#)]

60. Emil, M.K.; Sultan, M.; Alakhras, K.; Sataer, G.; Gozi, S.; Al-Marri, M.; Gebremichael, E. Countrywide Monitoring of Ground Deformation Using InSAR Time Series: A Case Study from Qatar. *Remote Sens.* **2021**, *13*, 702. [[CrossRef](#)]
61. Haley, M.; Ahmed, M.; Gebremichael, E.; Murgulet, D.; Starek, M. Land Subsidence in the Texas Coastal Bend: Locations, Rates, Triggers, and Consequences. *Remote Sens.* **2022**, *14*, 192. [[CrossRef](#)]
62. Rawat, M.; Joshi, V. Landslide Movement Monitoring Using GPS Technology: A Case Study of Bakthang Landslide, Gangtok, East Sikkim, India. *J. Dev. Agric. Econ.* **2011**, *3*, 194–200.
63. Borrelli, L.; Antronico, L.; Gullà, G.; Sorriso-Valvo, G.M. Geology, Geomorphology and Dynamics of the 15 February 2010 Maierato Landslide (Calabria, Italy). *Geomorphology* **2014**, *208*, 50–73. [[CrossRef](#)]
64. Conforti, M.; Ietto, F. An Integrated Approach to Investigate Slope Instability Affecting Infrastructures. *Bull. Eng. Geol. Environ.* **2019**, *78*, 2355–2375. [[CrossRef](#)]
65. Abedini, M.; Tulabi, S. Assessing LNRF, FR, and AHP Models in Landslide Susceptibility Mapping Index: A Comparative Study of Nojian Watershed in Lorestan Province, Iran. *Environ. Earth Sci.* **2018**, *77*, 405. [[CrossRef](#)]
66. Sidle, R.C.; Bogaard, T.A. Dynamic Earth System and Ecological Controls of Rainfall-Initiated Landslides. *Earth Sci. Rev.* **2016**, *159*, 275–291. [[CrossRef](#)]
67. Psomiadis, E.; Papazachariou, A.; Soulis, K.X.; Alexiou, D.S.; Charalampopoulos, I. Landslide Mapping and Susceptibility Assessment Using Geospatial Analysis and Earth Observation Data. *Land* **2020**, *9*, 133. [[CrossRef](#)]
68. Tagnon, B.O.; Assoma, V.T.; Mangoua, J.M.O.; Douagui, A.G.; Kouamé, F.K.; Savané, I. Contribution of SAR/RADARSAT-1 and ASAR/ENVISAT Images to Geological Structural Mapping and Assessment of Lineaments Density in Divo-Oume Area (Côte d’Ivoire). *Egypt. J. Remote Sens. Space Sci.* **2020**, *23*, 231–241. [[CrossRef](#)]
69. Yan, Y.; Doin, M.P.; López-Quiroz, P.; Tupin, F.; Fruneau, B.; Pinel, V.; Trouvé, E. Mexico City Subsidence Measured by InSAR Time Series: Joint Analysis Using PS and SBAS Approaches. *IEEE J. Sel. Top Appl. Earth Obs. Remote Sens.* **2012**, *5*, 1312–1326. [[CrossRef](#)]
70. Gido, N.A.A.; Bagherbandi, M.; Nilfouroushan, F. Localized Subsidence Zones in Gävle City Detected by Sentinel-1 PSI and Leveling Data. *Remote Sens.* **2020**, *12*, 2629. [[CrossRef](#)]
71. Fabio, I.; Massimo, C.; Cristiano, T.; Giuseppe, C. Village Relocation as Solution of the Landslide Risk, Is It Always the Right Choice? The Case Study of Cavallerizzo Ghost Village (Calabria, Southern Italy). *Int. J. Disaster Risk Reduct.* **2022**, *81*. [[CrossRef](#)]
72. Del Ventisette, C.; Righini, G.; Moretti, S.; Casagli, N. Multitemporal Landslides Inventory Map Updating Using Spaceborne SAR Analysis. *Int. J. Appl. Earth Obs. Geoinf.* **2014**, *30*, 238–246. [[CrossRef](#)]
73. Rosi, A.; Tofani, V.; Tanteri, L.; Tacconi Stefanelli, C.; Agostini, A.; Catani, F.; Casagli, N. The New Landslide Inventory of Tuscany (Italy) Updated with PS-InSAR: Geomorphological Features and Landslide Distribution. *Landslides* **2018**, *15*, 5–19. [[CrossRef](#)]
74. Trejo, R. Shoal Creek Landslide Area Still Eroding after 2018 Storms. Available online: <https://www.kvue.com/article/news/shoal-creek-landslide-area-further-eroding/269-aa60d787-4b72-41f7-9d7a-47d100596428> (accessed on 1 March 2024).
75. Cho, Y. Shoal Creek Landslide Area Damaged Even More after This Week’s Rain. Available online: <https://www.kxan.com/news/local/austin/shoal-creek-landslide-area-damaged-even-more-after-this-weeks-rain/> (accessed on 2 March 2024).
76. Garner, L.E.; Baker, V.R.; Turk, L.J.; Young, K. *Others Urban Flooding and Slope Stability, Austin, Texas*; Austin Geological Society (Texas): Austin, TX, USA, 1973.
77. Shi, X.; Jiang, H.; Zhang, L.; Liao, M. Landslide Displacement Monitoring with Split-Bandwidth Interferometry: A Case Study of the Shuping Landslide in the Three Gorges Area. *Remote Sens.* **2017**, *9*, 937. [[CrossRef](#)]
78. Cruden, D.M.; Varnes, D.J. Landslides: Investigation and Mitigation. Chapter 3—Landslide Types and Processes. 1996. Available online: <https://www.scirp.org/reference/referencespapers?referenceid=2624226> (accessed on 20 November 2022).
79. Hordyniec, P.; Kaplon, J.; Rohm, W.; Kryza, M. Residuals of Tropospheric Delays from GNSS Data and Ray-Tracing as a Potential Indicator of Rain and Clouds. *Remote Sens.* **2018**, *10*, 1917. [[CrossRef](#)]
80. Zhang, F.; Chen, W.; Liu, G.; Liang, S.; Kang, C.; He, F. Relationships between Landslide Types and Topographic Attributes in a Loess Catchment, China. *J. Mt. Sci.* **2012**, *9*, 742–751. [[CrossRef](#)]
81. Dille, A.; Kervyn, F.; Handwerker, A.L.; D’Oreye, N.; Derauw, D.; Mugaruka Bibentyo, T.; Samsonov, S.; Malet, J.P.; Kervyn, M.; Dewitte, O. When Image Correlation Is Needed: Unravelling the Complex Dynamics of a Slow-Moving Landslide in the Tropics with Dense Radar and Optical Time Series. *Remote Sens. Environ.* **2021**, *258*. [[CrossRef](#)]
82. Massey, C.I.; Petley, D.N.; McSaveney, M.J. Patterns of Movement in Reactivated Landslides. *Eng. Geol.* **2013**, *159*, 1–19. [[CrossRef](#)]
83. Wang, G.; Suemine, A.; Schulz, W.H. Shear-Rate-Dependent Strength Control on the Dynamics of Rainfall-Triggered Landslides, Tokushima Prefecture, Japan. *Earth Surf. Process Landf.* **2010**, *35*, 407–416. [[CrossRef](#)]
84. Chang, K.T.; Ge, L.; Lin, H.H. Slope Creep Behavior: Observations and Simulations. *Environ. Earth Sci* **2015**, *73*, 275–287. [[CrossRef](#)]
85. Hammons, A. Several Central Austin Homes near Edge of New Cliff after Shoal Creek Landslide | WOAI. Available online: <https://news4sanantonio.com/news/local/four-central-austin-homes-near-edge-of-new-cliff-after-shoal-creek-landslide> (accessed on 12 June 2022).
86. Federico, A.; Popescu, M.; Elia, G.; Fidelibus, C.; Internò, G.; Murianni, A. Prediction of Time to Slope Failure: A General Framework. *Environ. Earth Sci.* **2012**, *66*, 245–256. [[CrossRef](#)]
87. Abrams, T.G.; Wright, S.G. A Survey of Earth Slope Failures and Remedial Measures in Texas. 1972. Available online: <https://oa.mg/work/622524357> (accessed on 20 November 2022).

-
88. Hsu, S.C.; Nelson, P.P. Characterization of Eagle Ford Shale. *Eng. Geol.* **2002**, *67*, 169–183. [[CrossRef](#)]
 89. Wilkerson, M.; Larson, J.; Gaughan, M.; Marshall, D. A Unique Engineering Geology Approach to Aid in Design and Construction of a Pipeline Project in Texas. In Proceedings of the Pipelines 2013: Pipelines and Trenchless Construction and Renewals—A Global Perspective—Proceedings of the Pipelines 2013 Conference, Fort Worth, TX, USA, 23–26 June 2013.

Disclaimer/Publisher’s Note: The statements, opinions and data contained in all publications are solely those of the individual author(s) and contributor(s) and not of MDPI and/or the editor(s). MDPI and/or the editor(s) disclaim responsibility for any injury to people or property resulting from any ideas, methods, instructions or products referred to in the content.